POLITECNICO DI TORINO
Repository ISTITUZIONALE

Definition of a benchmark for low Reynolds number propeller aeroacoustics

Original
Definition of a benchmark for low Reynolds number propeller aeroacoustics / Casalino, D.; Grande, E.; Romani, G.; Ragni, D.; Avallone, F.. - In: AEROSPACE SCIENCE AND TECHNOLOGY. - ISSN 1270-9638. - 113:(2021), p. 106707. [10.1016/j.ast.2021.106707]

Availability:
This version is available at: 11583/2976698 since: 2023-03-14T11:05:38Z

Publisher:
Elsevier

Published
DOI:10.1016/j.ast.2021.106707

Terms of use:

This article is made available under terms and conditions as specified in the corresponding bibliographic description in the repository

Publisher copyright

(Article begins on next page)

12 October 2024

Aerospace Science and Technology 113 (2021) 106707

Contents lists available at ScienceDirect

Aerospace Science and Technology

www.elsevier.com/locate/aescte

Definition of a benchmark for low Reynolds number propeller aeroacoustics

Damiano Casalino [a], Edoardo Grande [b,*], Gianluca Romani [b], Daniele Ragni [b], Francesco Avallone [b]

[a] SIMULIA, Dassault Systèmes, Germany
[b] Aerodynamics, Wind Energy, Flight Performance and Propulsion Department, Delft University of Technology, the Netherlands

ARTICLE INFO

Article history:
Received 25 November 2020
Received in revised form 16 March 2021
Accepted 29 March 2021
Available online 9 April 2021
Communicated by Qiulin Qu

Keywords:
Propeller noise
Low Reynolds number propeller
BEMT
LBM
PowerFLOW
Aeroacoustic benchmark

ABSTRACT

Experimental and numerical results of a propeller of 0.3 m diameter operated at 5000 RPM and axial velocity ranging from 0 to 20 m/s and advance ratio ranging from 0 to 0.8 are presented as a preliminary step towards the definition of a benchmark configuration for low Reynolds number propeller aeroacoustics. The corresponding rotational tip Mach number is 0.23 and the Reynolds number based on the blade sectional chord and flow velocity varies from about 46000 to 106000 in the operational domain and in the 30% to 100% blade radial range. Force and noise measurements carried out in a low-speed semi-anechoic wind-tunnel are compared to scale-resolved CFD and low-fidelity numerical predictions. Results identify the experimental and numerical challenges of the benchmark and the relevance of fundamental research questions related to transition and other low Reynolds number effects.
© 2021 The Author(s). Published by Elsevier Masson SAS. This is an open access article under the CC BY license (http://creativecommons.org/licenses/by/4.0/).

1. Introduction

The development of tools for the design and optimization of propellers employed in multi-copter unmanned air vehicles and drones has to face two major difficulties. The first one is the availability of reliable force, flow and noise data acquired for the same experiment in controlled conditions. The second difficulty is related to the intrinsic limitation of scale-resolved CFD methods to capture low Reynolds number phenomena like laminar to turbulent flow transition and the occurrence of laminar separation bubbles.

Recent attempts to validate Lattice-Boltzmann Method / Very Large Eddy Simulation (LBM/VLES) results [1] revealed that the flow recirculation induced by a rotor operated in a confined environment, and the consequent interaction between blades and turbulent eddies, generates high-order Blade-Passing Frequency (BPF) loading noise harmonics. Similar observations have been made in other experiments [2]. Other sources of experimental uncertainties are: (i) the vibration of the test rig resulting in additional sources related to the random blade motion [3], (ii) the presence of electric motor noise, which is affected by the rotor torque [4] and thus not easily separable from the rotor aerodynamic noise, or treatable as a background noise contribution, and (iii) the flow regime at several radial stations (laminar/turbulent, attached/separated) and the presence of laminar separation bubbles. In the case of non-axial flow conditions, additional complications arise due to the periodic inflow variation and the necessity to characterize flow hysteresis mechanisms, while mitigating the higher vibrations of the rig. On the numerical side, the main challenges are related to the capability of the CFD solver to predict the correct transitional flow behaviour. Scale-resolved methods like LBM/VLES [5] or Detached Eddy Simulation [6] (DES), or different variants of hybrid Reynolds Averaged Navier-Stokes (RANS) / Large Eddy Simulation (LES) methods are typically used for aeroacoustic purposes as a faster alternative to LES. However, hybrid methods have to deal with the "grey-area" related problem of finding the balance between eddy viscosity in the scale-modelled flow region and the need of not anticipating separation on smooth surfaces, and not preventing transition in boundary layers and wakes [7,8]. Broadband noise is generated by the interaction between boundary layer turbulence and the trailing edge, by the impingement of inflow turbulence on the leading edge, and by Blade-Vortex Interaction (BVI) at very low or negative advance ratios. Trailing edge noise prediction, in particular, relies on the capability to predict transi-

* Corresponding author.
E-mail address: e.grande@tudelft.nl (E. Grande).

https://doi.org/10.1016/j.ast.2021.106707
1270-9638/© 2021 The Author(s). Published by Elsevier Masson SAS. This is an open access article under the CC BY license (http://creativecommons.org/licenses/by/4.0/).

tion with low-intrusive tripping devices like zig-zag strips [9,10] or synthetic turbulence generators [11].

Capturing the correct boundary layer properties of low Reynolds number propellers is also crucial for the sake of accurate thrust and torque predictions. Typical turbulence closure models used in RANS solvers suffer to predict the correct near-wall behaviour of turbulent flows and do not provide reliable predictive capabilities of transitional flows [12]. Low-fidelity methods based on the Blade Element Momentum Theory (BEMT) and two-dimensional airfoil lift and drag coefficients computed via coupled panel/boundary-layer models like Xfoil [13] can provide satisfactory accuracy, beyond the common expectation, at sufficiently high advance ratios [14]. Unfortunately, BEMT methods suffer for the inaccurate 2D prediction of stall and post-stall behaviour of highly loaded blade sections close to the hub at low advance ratios [15,16], and for the inaccurate modelling of the near-wake induction effects, again, at low advance ratios [14].

The main goal of the present work is to provide an overview of all the aforementioned experimental, numerical and modelling challenges by comparing preliminary experimental, scale-resolved LBM/VLES and low-fidelity BEMT results, and thus progress towards the definition of a benchmark problem for low Reynolds number propeller aeroacoustics. This is part of a research initiative aimed at investigating the different broadband noise generation mechanisms and the properties of transitional flows at different radial stations and for different operating conditions, including non-axial flow conditions that are typical of eVTOL vehicles and drones. More detailed descriptions of the experimental, numerical and modelling pillars of the present benchmark activity will be provided in future publications following the overview given in the present work.

The paper is organized as follows. The physical test environment and the propeller geometry are described in section 2. Information about the employed acoustic measurement techniques is provided in section 3. The LBM/VLES simulation framework based on the commercial CFD software SIMULIA PowerFLOW® by Dassault Systèmes (3DS) is described in section 4. In the same section, the Ffowcs-Williams & Hawkings (FW-H) tools available in the SIMULIA PowerACOUSTICS® software used to compute the noise from the transient near-field flow solution are also presented. The BEMT-based propeller noise formulation available in the *Opty∂B*® aeroacoustic toolkit by the first author is presented in section 5. Uncertainties and challenges characterizing the present benchmark are discussed in section 6. Experimental, low- and high-fidelity numerical results are reported, compared and discussed in section 7. Noise source analyses are presented in section 8. The main findings of the present work are finally drawn in the conclusive section.

2. Test rig and physical/digital environment

The test rig installed in the semi-anechoic aeroacoustic wind tunnel of Delft University of Technology (TU-Delft A-Tunnel) is shown in Fig. 1. In the present experiment, a convergent nozzle of contraction ratio 15:1 and exhaust diameter of 0.6 m is used. The maximum flow speed that the A-Tunnel is able to provide with this nozzle is 35 m/s, the mean streamwise velocity is uniform within 0.6%, the turbulence intensity is 0.14% at 2.5 m/s and decreases below 0.1% with a flow velocity above 10 m/s. The height of the test chamber is 3.2 m, and the other two dimensions are 6.4 m and 4.4 m. The cut-off frequency of the chamber is approximately 200 Hz. A description of the tunnel, with details of the flow and acoustic characterizations, can be found in Ref. [17].

The propeller is connected to a profiled aluminium cylindrical nacelle of 5 cm diameter for minimum interference with the propeller flow, within which the motor, an encoder, a load cell and a torque cell are embedded. The nacelle is supported by stiffened

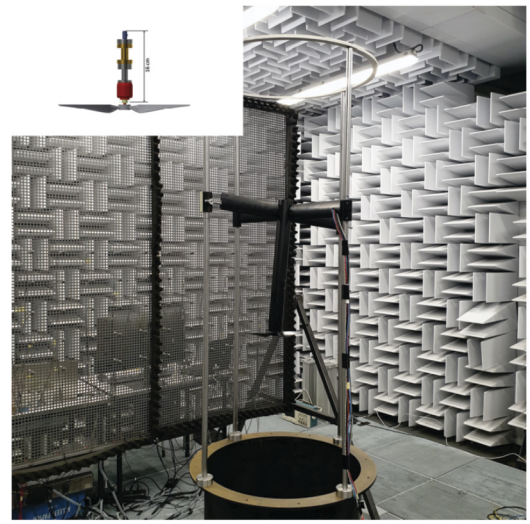

Fig. 1. Test rig in TU-Delft A-Tunnel.

hollow aluminium NACA 0012 profiles of 6 cm chord, inside which the cabling is housed and remotely connected to the instrumentation. The entire structure is held up above the nozzle of the tunnel by four wire tubes of 2 cm diameter fixed to the tunnel. The entire rig is very stiff and submitted to almost no vibration when the rotor is operated in axial flow conditions, as in the present preliminary campaign. The nacelle hosts the propeller drivetrain, which consists of:

- an electrical brushless motor Leopard Hobby 3536-5T 1520 KV with a diameter of 27.8 mm and maximum power of 550 W;
- a US Digital EM1 optical encoder to measure the shaft rotational speed, which consists of a rotating disk, a light source and a photo detector;
- a load cell Futek LSB200 excited with 5 VDC for the thrust measurement, and characterized by a maximum capacity of 22.2 N, non-linearity and hysteresis of ±0.1% of RO and an operating temperature range of 223–365 K;
- a Transducer Techniques RTS-25 torque sensor excited with 10 VDC, characterized by a maximum capacity of 0.18 Nm, non-linearity and hysteresis of ±0.1% of RO and an operating temperature range of 219–366 K.

The motor is powered by a Delta Elektronika DC power supply with a voltage range of 0–15 V and a current range of 0–100 A. The distance between the rotor plane and the jet exhaust plane is about 0.5 m. The thrust and torque signals are acquired by a National Instrument acquisition board with a sampling frequency of 5 KHz and an acquisition time of 15 s. An exploded view of the propeller drivetrain is shown in Fig. 2.

The present test rig has been designed to host a PIV acquisition system for rotor phase-locked acquisition, and to enable non-axial flow aeroacoustic studies by pivoting the whole system. These aspects will be the subject of future publications.

The propeller employed for this experiment is derived from a two-bladed APC-96 model, by reshaping each single profile with a NACA4412 airfoil and rescaling the size to $D = 0.3$ m rotor diameter (tip radius $R_T = 0.15$ m). An elliptical root section is merged with the profiled section starting from a radius of 1 cm ($r/R_T = 6\%$). The hub radius is 1.25 cm. An image of the propeller together with the employed reference system is shown in Fig. 3. The chord and twist radial distribution are plotted in Fig. 4. The propeller, made of aluminium alloys, was manufactured using CNC machining with Ra surface finish between 0.4 to 0.8 μm. The in-

Fig. 2. Exploded view of the propeller drivetrain.

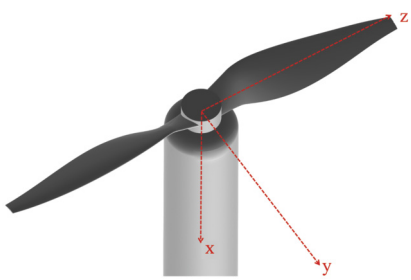

Fig. 3. Propeller geometry and reference system.

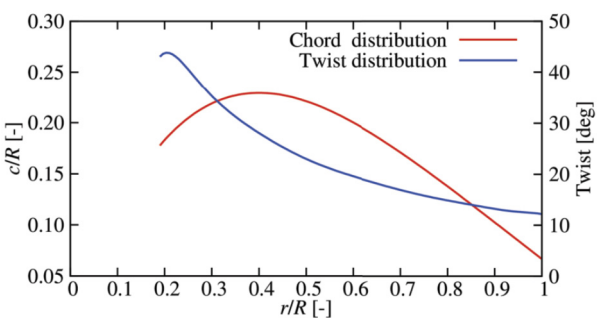

Fig. 4. Propeller chord and twist distributions. (For interpretation of the colours in the figure(s), the reader is referred to the web version of this article.)

terest of using this model instead of the original off-the-shelf one resides in: (i) the possibility to deliver a CAD model and the analytical description of the constructive parameters as part of the benchmark definition, (ii) the possibility to control manufacturing tolerances, (iii) and the high stiffness of the model, thus guaranteeing negligible elastic deformations in operation.

The propeller is located about 1.2 nozzle diameter from the nozzle, thus well inside the potential core of the jet. This prevents the occurrence of noise generated by the interaction between the rotor blades and jet shear-layer instabilities, as well as spectral broadening of noise tones due to random variations of the acoustic travel time across the unsteady jet shear layer. As discussed in section 6.4, flow simulations are conducted by considering a propeller in free-stream conditions. The finite extension of the jet, whose cross sectional area is only four times larger than the rotor area, is expected to have an influence on the rotor steady loading, and thus on the noise BPF tone. This effect will be quantified in future studies by comparing free-stream and jet-stream simulations results, in particular for cases at non-zero inflow angle. Indeed, when the rotor plane is tilted, the jet deflection and distortion induced by the propeller are expected to have a non negligible effect on the periodic blade loading, and thus on tonal noise BPF harmonic components.

Table 1
Propeller operating conditions.

V_0 (m/s)	J	Re_{min}	Re_{max}
0	0	46400	96700
6	0.24	52100	98200
10	0.4	56300	99700
15	0.6	63000	102800
20	0.8	68400	105600

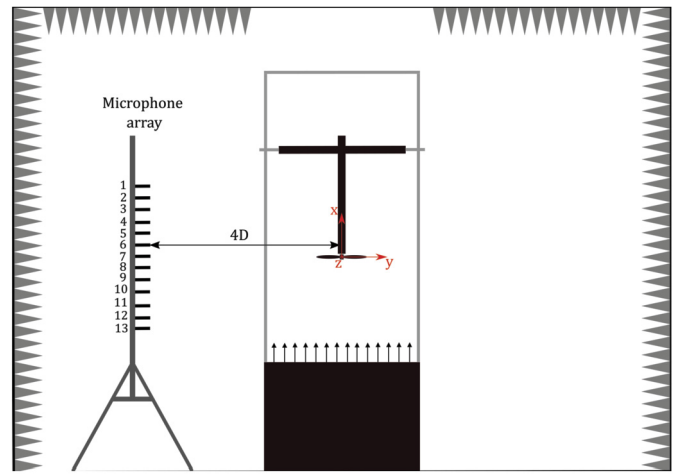

Fig. 5. Linear microphone array configuration.

The propeller is operated by varying the jet wind tunnel velocity and the motor RPM to obtain a range of advance ratio $J = V_0/(nD)$ from 0 to 0.8, V_0 denoting the free-stream axial flow velocity and n the number of rotor revolutions per second. In the present work, only results for five values of the jet exit velocity of 0, 6, 10, 15 and 20 m/s, 5000 RPM (rotational tip Mach number of 0.23) and zero flow incidence are considered, corresponding to $J = 0$, 0.24, 0.4, 0.6, and 0.8, respectively. Notice that BEMT computations are performed with a step of 2 m/s of the axial velocity (11 conditions), therefore the advance ratio value of 0.6 is replaced by a value of 0.64 ($V_0 = 16$ m/s). Acoustic results are not reported for $J = 0.8$, since the propeller thrust and thus the tonal noise vanish, while the wind-tunnel background noise overwhelms the broadband rotor noise.

A summary of the operating conditions and corresponding minimum and maximum Reynolds number based on the sectional chord and total velocity computed by BEMT is reported in Table 1.

It is worth mentioning that, due to very low values of the jet Mach number (0.06 at $J = 0.8$), no shear-layer corrections are needed to take into account the effects of the mean-flow refraction on the radiated noise levels and directivity.

3. Noise measurements

Noise measurements are performed through 13 G.R.A.S. 40PH analog free-field microphones (frequency response: ±1 dB in the frequency range of 10 Hz to 20 kHz, maximum output: 135 dB) mounted on a linear microphone array, sketched in Fig. 5, located in a plane perpendicular to the propeller plane. The array is at 1.2 m ($4D$) in the y direction with respect to the propeller axis. The distance between each microphone is 0.15 m ($0.5D$), the microphone #7 is located at the propeller plane, the microphone #1 is 0.9 m ($3D$) above the propeller plane and the microphone #13 is 0.9 m below. The microphone mounting supports and array frame

are covered by a layer of acoustic absorbing material in order to mitigate the acoustic reflections.

The data acquisition system consists of two National Instrument modules NI9234. A sampling frequency of 51.2 kHz and a recording time of 30 s are used for each measurement. The acoustic signals are separated into 1197 Hanning-widowed Welch blocks with 50% overlap, corresponding to a bandwidth of 20 Hz.

After every change of the inflow velocity, noise acquisitions are started after a sufficiently long time to achieve stabilized pressure conditions in the chamber. Flow recirculation around the propeller is monitored with a hot-wire scanning at different axial and radial locations. Spurious effects related to the flow recirculation will be addressed in future studies.

4. LBM/VLES flow solver and FW-H tools

The SIMULIA PowerFLOW solver, version 6-2019, has been used in the present work. The properties of this software and its suitability for aeroacoustic applications are widely discussed in the literature, covering both aerospace, automotive and wind-energy applications. Referring to noise from rotating parts, the following benchmark works can be quoted: small UAV rotors [1], car cooling fans [18], aircraft propellers [19], aero-engine fan/OGV stages [10,9,20], and helicopter rotors [21]. PowerFLOW is based on a Cartesian mesh LBM with automatic mesh generation, with no restriction on the geometric complexity of the models that can be treated. Fully automatic workflows, from case preparation to results post-processing, can be easily developed, as for complex thrust-vectoring multi-copter eVTOL vehicles [5], for which an entire flight envelop can be explored in reasonable times by running multiple jobs on a HPC cloud system.

LBM is intrinsically unsteady and compressible. It is based on the idea of statistically tracking the advection and collisions of fluid particles by an integer number of distribution functions aligned with predefined discrete directions. Flow variables such as density and velocity are computed by taking the appropriate moments, i.e., summations over the set of discrete directions of the particle distribution function [22]. The relaxation time and other parameters of the equilibrium distribution function are computed by considering scales related to the turbulent motion of the resolved flow field, computed using a two-equation transport model based on the $k-\epsilon$ re-normalization group theory [23,24]. Conversely to RANS models, Reynolds stresses are not explicitly added to the flow governing equations, but are a consequence of an alternation of the gas relaxation properties that lead the flow towards a state of dynamic equilibrium. This is the essence of the LBM/VLES model: an extension of the kinetic theory from a gas of particles to a gas of eddies, which can be also interpreted as the application of a Boussinesq model at lattice Boltzmann level. It can be demonstrated that the effective Reynolds stresses have a non-linear structure and are better suited to represent turbulence in a state far from equilibrium, such as in the presence of distortion, shear and rotation [25].

The noise radiated at the microphone positions is computed in a post-processing stage by using three softwares, two are based on a standard FW-H Formulation 1A by Farassat [26], solved in forward-time [27] and performing the integration on the solid surfaces of the propeller, and one is based on the frequency formulation for non-moving sources by Lockard [28] extended to three dimensions. The first software is PowerACOUSTICS, and it is used to compute the reference signals and spectra compared to the measurements and low-fidelity predictions, whereas the second and third software are part of the *Opty∂B* toolkit embedded in the automatic eVTOL aeroacoustic PowerFLOW workflow. The two time-domain FW-H software compute identical noise signals, but the second one, *Opty∂B*-PFNOISESCAN, gives access to additional noise source information through the following list of features used for the present work:

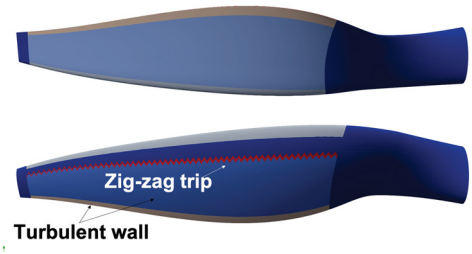

Fig. 6. Digital propeller model with wall partitioning and trip on the suction side.

- beam-forming analysis in the rotating reference system for broadband noise source analysis;
- visualization of the surface noise contribution at a given instant and microphone.

The frequency-domain FW-H software *Opty∂B*-FWHFREQ is used to compute noise spectra in the reference system of the blade at hundreds of microphone on a digital beam-forming array used to perform beam-forming visualization of broadband noise sources. The CLAEN-SC [29] algorithm available in *Opty∂B*-BF, benchmarked against other CLEAN-SC implementations [30].

The 3DS automatic eVTOL noise PowerFLOW workflow has been used for the present study. The workflow is fed with one blade STL file, a hub STL file, and, if present, an airframe STL file. This guarantees a user-friendly access to a multi-fidelity approach in 3DS model-based system engineering framework for eVTOL flight mechanics and community noise assessment. In the PowerFLOW workflow, the user prescribes ambient and flight conditions, rotor settings (centre, axis, RPM) and, if required, reference thrust value for an automatic collective/cyclic pitch trim of the rotor. The blade geometry file is processed by the *Opty∂B*-PFROTOR that generates: a blade portion for the setting of laminar/turbulent patches and the generation of mesh refinement regions, a zig-zag trip on the suction and/or pressure side of the blade, and a structured mesh for advanced force/noise post-processing. Interestingly, the same tool *Opty∂B*-PFROTOR used to process the blade geometry is also used to generate all the input files required by the fully analytical BEMT-based force/noise prediction workflow. The PowerFLOW workflow creates a simulation setup from scratch, following an established best practice in terms of mesh resolution and solution sampling properties. Once the simulation is completed, the workflow executes the tool *Opty∂B*-PFPROP to perform standard and advanced force/noise analyses, community noise assessment for a user defined trajectory, and sound auralization. For the sake of the present analysis, a zig-zag trip of 0.17 mm height is located at 25% of the chord on the suction side only. As depicted in Fig. 6, the trip separates a wall-modelled laminar-to-turbulent automatic transition patch from a wall-modelled fully-turbulent patch. An automatic laminar-to-turbulent transition model is used on the other partitions. The finest mesh resolution of 5200 voxels/D is used around the leading- and trailing-edge and the trip, whereas a twice coarser mesh resolution is used elsewhere around the blade. The grid dependence of both forces and far-field noise is discussed in section 6.4. The trip height is resolved with about 3 voxels. Based on the empirical criteria of a height-based critical Reynolds number of 200 [31], the trip is about 6 times higher than the critical one for the hover case and a radial section $r/R_T = 85\%$. For the same condition, the trip height in viscous units (y^+) varies from about 15 at $r/R_T = 30\%$ to about 50 at the tip. Therefore, a boundary layer transition simulation would be over-tripped, but in the present case the trip is only expected to drive the VLES model to-

wards a scale-resolving behaviour, and in this respect it is not very intrusive. To support this argument, a sensitivity study of the radiated acoustic field to the trip height is reported in section 6.4.

Several simulations have been carried out with the goal of investigating the effect of the trip location on aerodynamic forces and noise, which will be extensively described in future publications. More specifically, simulations for all the aforementioned values of the advance ratio have been also conducted with a trip following the transition line predicted by the BEMT method. The results show only a small reduction of the broadband noise levels, as a consequence of a delayed unforced transition at increasing advance ratios. An example of noise spectrum predicted with the two trip locations is also reported in section 6.4.

To conclude this section, some information about the simulation setup is provided. A free-stream representation of the problem is considered, therefore the wind-tunnel nozzle, the jet flow and the different components of the test rig are not included in the simulation. A fully anechoic environment is simulated, by considering a spherical simulation domain of $325D$ radius, with the rotor located in the centre, and by applying acoustic sponges starting from a distance of $15D$ from the rotor. The overall number of finest-equivalent voxels is 15.2 million and every run, consisting of 8 and 10 rotor revolutions for settling and acquisition, respectively, requires about 27 h on 430 Intel Xeon CPU E5-2697 2.6 GHz processors.

5. BEMT-based model

A conventional BEMT formulation with uniform inflow and Prandtl tip-losses correction is employed. The required blade sectional forces are computed using the boundary layer model by Drela & Giles [32,13] implemented in the BEMT tool. Aerodynamic polars are pre-computed with an angular step of 1 deg in the angle of attack range from $-16°$ to $16°$, and at five values of the Reynolds number covering the whole range of radial variation. For the sake of numerical robustness and efficiency, all quantities employed by the iterative BEMT algorithm (sectional aerodynamic coefficient and stall angles) and by the broadband noise model (boundary layer properties at the trailing edge) are polynomially fitted with respect to the radial coordinate and the angle of attack. Post-stall lift and drag coefficients are computed using the Viterna & Corrigan approach [33].

A crucial element of the developed BEMT procedure consists in the way the iterative axial and azimuthal momentum balance is applied. Following the classical BEMT procedure, the equilibrium for a circular radial strip of size Δr reads:

$$\Delta T = 4\pi r \rho_\infty V_\infty^2 (1+a) a \Delta r = \frac{1}{2}\rho_\infty V_1^2 c (c_l \cos\phi - c_d \sin\phi) B \Delta r \tag{1}$$

$$\begin{aligned}\Delta Q &= 4\pi r^3 \rho_\infty V_\infty \Omega (1+a) b \Delta r \\ &= \frac{1}{2}\rho_\infty V_1^2 c (c_d \cos\phi + c_l \sin\phi) B r \Delta r,\end{aligned} \tag{2}$$

where c is the blade sectional chord, B is the number of blades, a is the axial velocity induction coefficient ($V_x = V_\infty(1+a)$), b is the azimuthal velocity induction coefficient ($V_t = \Omega r(1-b)$), $V_1 = \sqrt{V_x^2 + V_t^2}$ is the total velocity seen by every radial section, and $\phi = \tan^{-1}(V_x/V_t)$ is the flow induction angle. The local flow incidence as a result of the geometrical blade section pitch θ and wake induction is $\alpha = \theta - \phi$. The sectional lift and drag coefficients c_l and c_d are function of the local α, Reynolds and Mach number, and are computed from stored look-up tables of polynomial fitting coefficients. By introducing the radial solidity coefficient $\sigma = cB/(2\pi r)$, the sectional thrust and torque coefficients $c_T = c_l \cos\phi - c_d \sin\phi$ and $c_Q = c_d \cos\phi + c_l \sin\phi$ and simplifying, it is possible to obtain the following two equations:

$$(1 - \frac{\sigma}{4} c_T) a^2 + (1 - \frac{\sigma}{2} c_T) a - \frac{\sigma}{4} c_T 1 + \frac{\Omega r}{V_\infty}^2 (1-b')^2 = 0 \tag{3}$$

$$b = \frac{\sigma}{4} \frac{V_\infty^2 (1+a)^2 + \Omega^2 r^2 (1-b')^2}{V_\infty \Omega r} \frac{c_Q}{1+a}. \tag{4}$$

This system of algebraic equations is solved iteratively, b' demoting the value of b at the previous iteration, with initial guess values of 0.2 and 0.1 for a and b, respectively, using a relaxation coefficient of 0.3, and by considering the largest positive root of the second order equation for a. This procedure allows a to exceed the unitary value at low advance ratios.

Integration of the sectional thrust and torque coefficient along the radial extension of the blade, from a minimum radius to the tip radius R_T provides the overall thrust and torque which are subsequentially translated into thrust and torque coefficients C_T and C_Q by dividing by $\rho_\infty \Omega^2 \pi R_T^4$ and $\rho_\infty \Omega^2 \pi R_T^5$, respectively. Results reported in section 7 have been obtained by integrating the forces from $r/R_T = 0.3$ to 1.

The radial distribution of the blade sectional force and the sectional airfoil surface are used to define the input of a time-domain FW-H noise computation based on the compact dipole and monopole formulation by Casalino et al. [34]. This provides the tonal noise contribution, whereas broadband noise is computed using the trailing edge noise model by Roger & Moreau [35], extended to a rotating blade [36] and by using seven different semi-empirical Wall Pressure Spectrum (WPS) models based on boundary layer quantities extracted at 95% of the chord. The employed WPS models are:

- Schlinker & Amiet [37], based on boundary layer edge velocity and displacement thickness;
- corrected Schlinker & Amiet, where the exponent of the correction function (equation A6 in Ref. [38]) has been multiplied by an arbitrary factor 5;
- Goody [39], based on boundary layer edge velocity, thicknesses, and skin shear stress;
- Rozenberg-07 [40], derived from Goody model, based on boundary layer edge velocity, thickness, displacement and momentum thicknesses, skin shear stress and streamwise pressure gradient;
- Rozenberg-12 [41], derived from Rozenberg-07 model;
- Kamruzzaman et al. [42], derived from Goody model, based on boundary layer edge velocity, displacement and momentum thicknesses, skin shear stress and streamwise pressure gradient;
- Lee [43], derived from Rozenberg-12 model.

A similar broadband noise prediction procedure for rotor/propeller assessment and optimization has been used by other authors in the past [44,45].

6. Sanity checks

In this section, possible causes of discrepancy between the three approaches involved in the current benchmark are investigated with the goal of assessing the level of maturity of the current benchmark before further steps. A mutual comparison between predictions and measurements repeated at different times is indeed the best way to progressively increase the quality of the dataset prior realising it to the community.

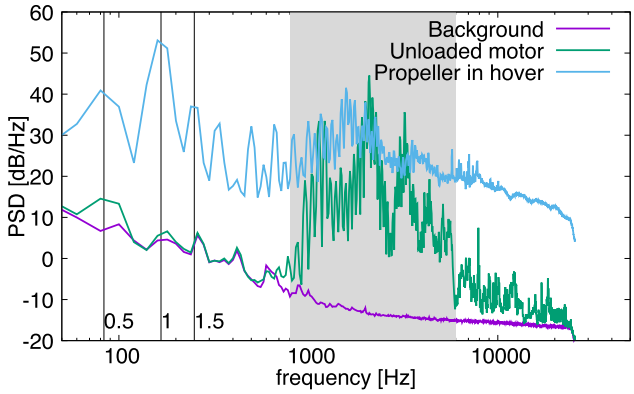

Fig. 7. Background, electric motor and propeller noise in hover conditions at microphone #7, with vertical lines marking BPF harmonics.

6.1. Experimental challenges and uncertainties

The reported experiment constitutes a repetition of a previous one described in Ref. [46], after which an amplitude modulation in the noise spectra was observed, due to reflections on the microphone array. In the current experiment, the previous circular array has been replaced by a linear array, and acoustic absorbing material has been applied around the microphones to mitigate reflections. This new experiment offers the occasion to investigate the effects of free-/fixed-transition point on the blade by performing noise measurements with/without a transition strip applied to 25% of the chord on the blade suction side. Although acoustic reflections have been significantly removed, other previously identified sources of uncertainty remain and are currently scrutinized in preparation of future measurement campaigns. These are reported in the following paragraphs.

- Instantaneous variation of the propeller RPM. A statistical analysis of the BPF tonal level was conducted and led to the observation that a variance of about 1 dB can be expected over the whole operational range and radiation arc, and up to about 2 dB in two cases: (i) hover, due to the higher forces, and (ii) at $J = 0.8$, due to the higher impact of the inflow velocity fluctuations.
- Presence of rotor motor noise, which has been identified through motor-alone noise measurements in high-frequency tonal peaks in the range of 1 to 6 kHz, as evident in the noise spectrum PSD plotted in Fig. 7.
- Presence of a shaft frequency peak (BPF= 0.5) and harmonics due to an imperfect balance of the blades in high load conditions, as also evident in Fig. 7. It should be pointed out that motor-alone noise measurements in loaded conditions can also reveal the presence of intense harmonics of the shaft frequency.
- Presence of background wind-tunnel noise below the cut-off frequency (~ 200 Hz). As discussed in Ref. [46], the wind-tunnel noise masks the BPF tonal peak at $J = 0.8$. Therefore, noise results for this condition are not reported in this work. At lower advance ratios a sufficient signal-to-noise ratio exists, but the noise level at the first BPF (167 Hz) is submitted to a certain uncertainty.
- Location of the boundary layer transition at different operating conditions, especially for the untripped cases.

A more detailed description of the experimental facility and uncertainty characterization is the subject of future publications.

6.2. Verification of airfoil boundary layer analytical solution

The main challenge in a BEMT analytical approach consists in computing the correct aerodynamic polar and boundary layer properties, including transition, laminar and turbulent separation. In this work we have adopted the boundary layer model by Drela & Giles [32], coupled with a 2nd order panel method through an iterative process based on the boundary layer transpiration velocity. A specific feature of the implemented algorithm is the management of the Lighthill's singularity close to laminar separation, which consists in assuming a vanishing streamwise gradient of the kinetic energy shape parameter, providing a value of the edge velocity gradient, and making use of de l'Höpital theorem. Performing a validation of the model is beyond the scope of the present work, but it is interesting to perform a verification of the implementation by using Xfoil results as a reference. A NACA4412 profile discretized with 160 panels clustered at the leading edge and a blunt trailing edge of thickness $t/c = 2.52 \cdot 10^{-3}$ is used. Polar computations have been performed for a Mach number of 0.1 and two values of the Reynolds number, 10^6 and $8 \cdot 10^4$, the second one being in the average range of the present propeller analysis.

Fig. 8 shows the aerodynamic lift and drag coefficients computed with Xfoil and with *Opty∂B*-BEMT. At high negative angles of attack, the Xfoil results have not reached convergence and no attempt was done to prevent this. At the higher value of the Reynolds number the agreement between the two codes is fair, whereas, at the lower Reynolds number, a significant difference can be observed, in particular in the drag coefficient.

Boundary layer properties for the Reynolds number equal to 10^6 are plotted in Figs. 9 and 10 for an angle of attack of 4° and 12°, respectively. At $\alpha = 4°$, the most significant difference between the two results is the location of the transition, which is anticipated by about 10% by *Opty∂B*-BEMT. At this Reynolds number, both solutions reveal the presence of a trailing-edge turbulent separation on the suction side at the higher angle of attack, but the displacement thickness after separation undergoes a slower growth in the *Opty∂B*-BEMT solution. Consequently, the displacement and momentum thickness follow a different development in the wake. These differences are related to the underestimated drag at high positive angle of attack observed in Fig. 8.

Boundary layer properties for the Reynolds number of $8 \cdot 10^4$ are plotted in Figs. 11 and 12 for an angle of attack of 4° and 12°, respectively. At $\alpha = 4°$, a laminar separation bubble on the suction side takes place in both solutions, but its extension is smaller for the *Opty∂B*-BEMT solution. Furthermore, the *Opty∂B*-BEMT solution exhibits a significantly lower growth rate of the displacement thickness in the bubble. Similar trends can be observed at 12° incidence, although the influence of the laminar bubble on the different evolution of the boundary layer after reattachment is smaller than at lower incidence. A trailing-edge turbulent separation can be observed also for this Reynolds number, and it is characterized by a faster growth of the momentum thickness predicted by *Opty∂B*-BEMT. At this angle of attack, the trends in the wake are also very different and deserve more attention in the future.

It is important to mention that the existence of laminar separation bubbles has been observed also for the present propeller case through phase-locked PIV measurements and oil flow visualizations, which will be described in future publications. An hypothesis is therefore under examination, according to which the high frequency humps observed in the noise spectra are associated with the near wake shedding originated from a laminar separation bubble [47,48]. As discussed in section 7, the comparison between the noise spectra measured for a clean and a tripped propeller is very useful to shed some light on this flow mechanism.

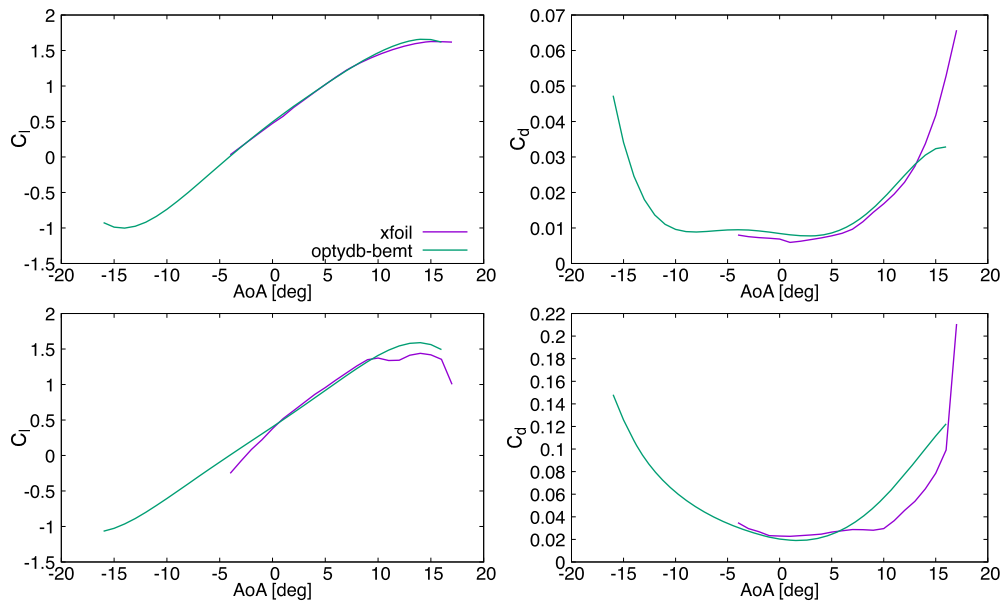

Fig. 8. Aerodynamic coefficients for Reynolds number of 10^6 (top) and $8 \cdot 10^4$ (bottom).

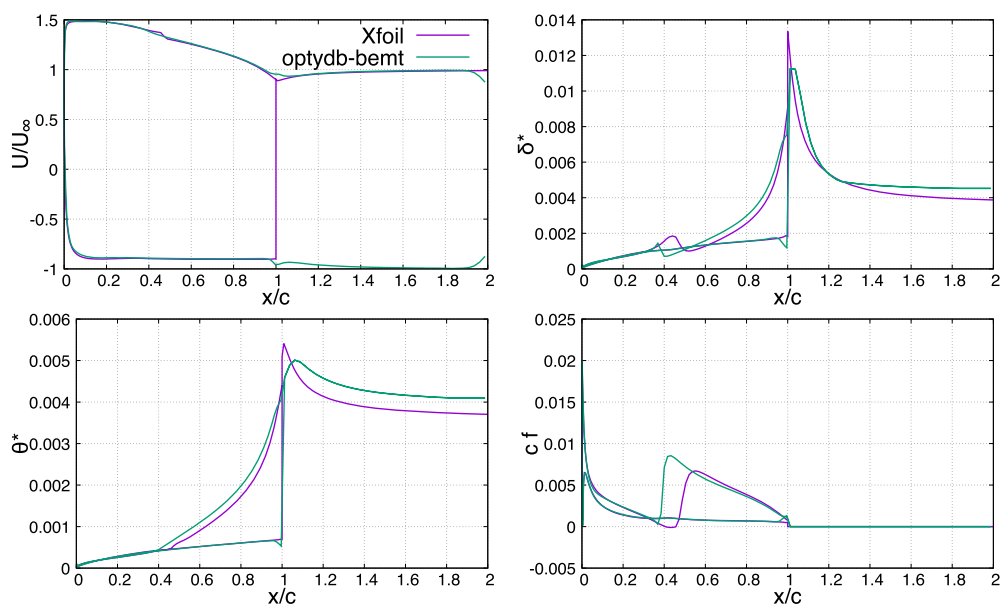

Fig. 9. Boundary layer edge velocity, displacement thickness, momentum thickness and skin friction coefficient for Reynolds number of 10^6 and $\alpha = 4°$.

6.3. Selection of the trailing-edge noise model

A pre-comparison between measured noise spectra and BEMT-based trailing-edge noise prediction carried out using the tool *Opty∂B*-PNOISE is performed with the goal of selecting the best WPS model for the present propeller. All computations have been performed by considering a convection velocity coefficient of 0.65 and a spanwise correlation coefficient of $b_c = 1.5$ in Roger & Moreau's formulation, without any further tuning. Fig. 13 shows comparison between the aforementioned seven models and the measured noise spectra. Unfortunately, part of the relevant frequency range is contaminated by the electric motor noise. Moreover, as it will be discussed in section 7, the measured noise spectra at $J = 0.4$ and $J = 0.6$ reveal the presence of a high-frequency hump, which is likely due to a laminar separation bubble. It is therefore not easy to perform a method assessment. For all advance ratios, all the Goody-like models provide similar trends, but significantly different levels, in line with previous calculations [43]. In hover conditions, the Rozenberg-07 model overestimates the noise levels by more than 20 dB, and this is likely due to a stronger sensitivity to the wall pressure gradient. Based on these results, it can be argued that the corrected Schinkler & Amiet's model provides slightly better spectral trends, and significantly better noise level prediction for all conditions. In section 7, only the corrected Schinkler & Amiet's WPS model results will be compared to the LBM/VLES results. It is worth pointing out that the employed trailing-edge noise model includes a leading-edge back scattering correction based on the leading term of the Schwarzschild's solution. Nevertheless, it is expected to be less reliable in the low Helmholtz number range, say for acoustic wavelengths much larger than the airfoil chord.

6.4. LBM-VLES simulation grid independence and trip effects

The PowerFLOW setup used in this study has been already used for a wide class of propeller/rotor aerodynamic and aeroacoustic simulations. Based on the acquired experience, the main sources

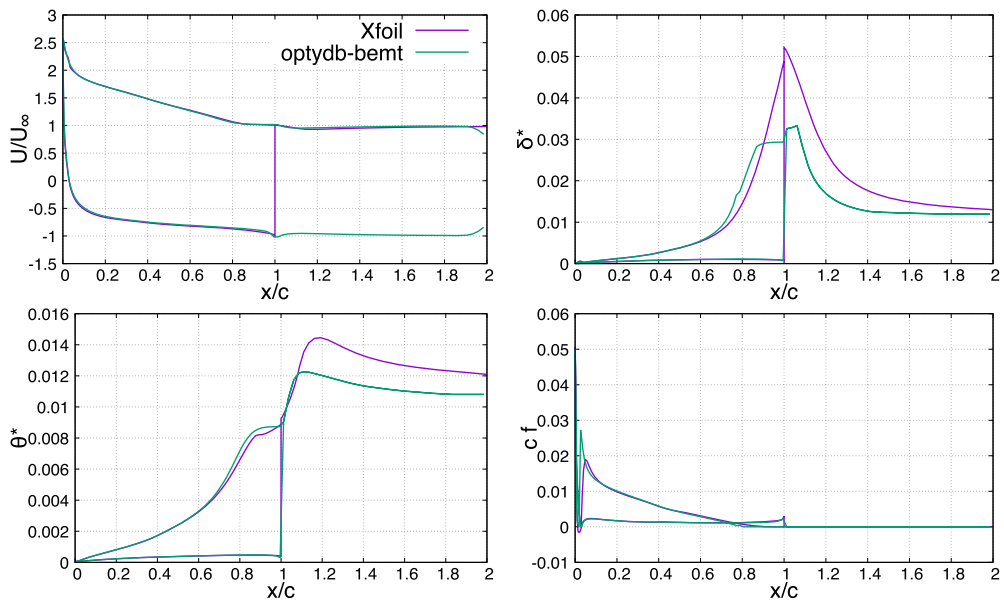

Fig. 10. Boundary layer edge velocity, displacement thickness, momentum thickness and skin friction coefficient for Reynolds number of 10^6 and $\alpha = 12°$.

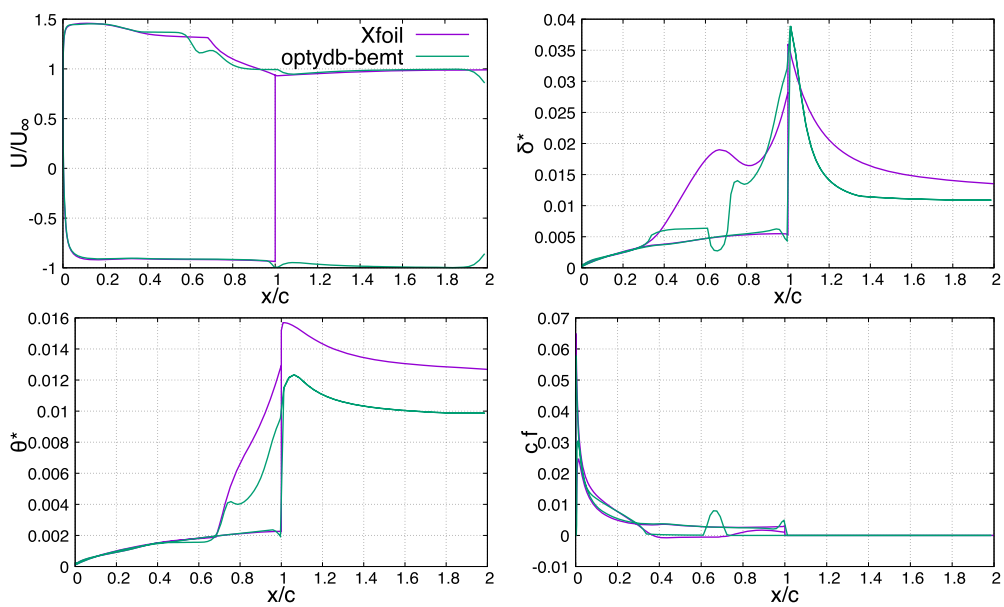

Fig. 11. Boundary layer edge velocity, displacement thickness, momentum thickness and skin friction coefficient for Reynolds number of $8 \cdot 10^4$ and $\alpha = 4°$.

of numerical uncertainty are the mesh resolution and the trip location.

Concerning the first one, a best practice has been established, which is based on the Reynolds number, but it is always useful to perform a mesh resolution study. Fig. 14 shows the grid convergence trend of the force coefficients for an intermediate value of the advance value, and noise spectra at a microphone located in the rotor plane. The employed grid refinement ratio is $\sqrt{2}$, with 1 and 2 corresponding to the coarse and fine resolution level, respectively. Grid independence of forces is clearly reached with a medium resolution, the fine one being the best practice value for the present Reynolds number. In terms of noise, the tonal contributions are also converged at medium level, whereas a convergence margin of about 2 dB can be observed in the high-frequency broadband levels. The results, however, exhibit an asymptotic convergence towards lower SPL values.

In order to investigate the effects due to the trip location, also in connection with the transitional regime of the untripped/tripped propeller measurements, simulations have been performed for all advance ratios considering two trip locations: 25% of the chord, and a transition line predicted by the BEMT tool. Fig. 15 shows the comparison of the SPL spectrum at microphone #7 for two values of the advance ratio and the two different locations of the trip. The BEMT-predicted transition lines are also plotted. For both values of the advance ratio, the influence of the transition location on the BPF tonal level is negligible. For the case $J = 0.24$ the transition location along the blade span varies between 45% and 60% of the chord and the effect of the trip location is in the order of 1 dB. Conversely, for the case $J = 0.6$ the transition location is above 75% of the chord and the broadband noise spectrum exhibits a level difference up to about 10 dB, which is of course due to the large difference in the trip location. Very interestingly, at $J = 0.6$, due to the noise hump induced by the laminar separation bubble in the untripped blade tests, simulations and measurements exhibit an opposite trend.

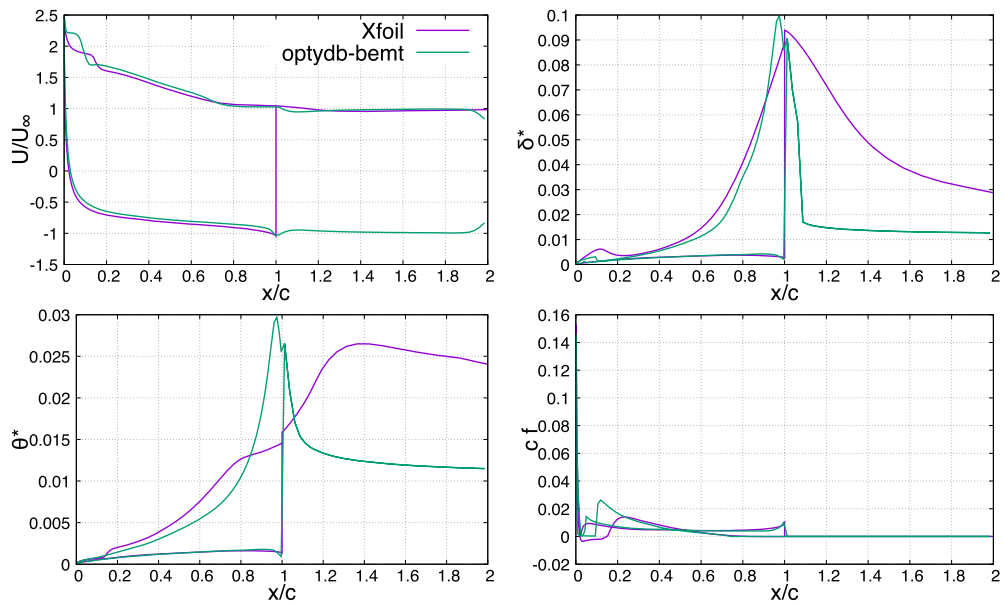

Fig. 12. Boundary layer edge velocity, displacement thickness, momentum thickness and skin friction coefficient for Reynolds number of $8 \cdot 10^4$ and $\alpha = 12°$.

7. Benchmark results

In this subsection a subset of low- and high-fidelity results are compared to available experimental data. Unless otherwise stated, both low- and high-fidelity results are obtained by tripping the blades at 25% of the chord.

Prior to the different comparisons, it is interesting to present some qualitative PowerFLOW solution. Fig. 16 shows iso-surfaces of λ_2 (value $-1.5 \cdot 10^6$ $1/s^2$), coloured by vorticity magnitude in the range from 0 to 10^4 s^{-1}, for the case $J = 0.4$. A well developed turbulent boundary layer trigged by the zig-zag trip can be observed on the blade suction side.

Contour plots of the time-average velocity magnitude in a meridian plane are shown in Fig. 17 for three values of the advance ratio. Interestingly, for the highest value $J = 0.8$, the slipstream velocity is very close to the free-stream value, which corresponds to a condition of zero thrust. Instantaneous vorticity magnitude on the same plane is shown in Fig. 18. The typical tip-vortex pattern with trailing and blade junction vortices is visible. For the hover condition ($J = 0$), the rotor wake is less organized and the occurrence of weak BVI can be observed.

Results of thrust and torque coefficients are shown in Fig. 19 and 20. Compared to experiments, thrust is predicted in a satisfactory way over the whole advance ratio range, and the agreement between low- and high-fidelity results is quite satisfactory, even close to hover conditions, for which BEMT is typically not very accurate. The zero-thrust condition around $J = 0.8$ is also well predicted by both LBM/VLES and BEMT. Overall, the three data sets exhibit thrust and torque values in fairly good agreement. In a future deployment of the present aeroacoustic benchmark, it will be interesting to measure forces with a different apparatus and in a different wind tunnel, and to compare the current predictions with other CFD and low-order methods.

Noise spectra at two reference microphones #1 (ground) and #7 (rotor plane) are shown in Fig. 21. Low- and high-fidelity predictions are compared to untripped blade measurements.

Tonal noise is initially inspected. Consistently with the force prediction, the BEMT-based noise model in *Opty∂B*-PNOISE is able to predict accurate BPF tone peaks that compare fairly well with the LBM/VLES prediction for the four values of the advance ratio. Both numerical predictions systematically underestimate the BPF tone peak, but, as pointed out in section 6.1, the test chamber cut-off frequency is in the order of 200 Hz, and it is therefore reasonable to expect a non negligible acoustic confinement effect. The measured spectra in hover exhibit higher tones at BPF harmonics. A similar behaviour was reported in past studies [1]; it was correlated to the occurrence of blade loading unsteadiness induced by the interaction between the blade lading edge and inflow perturbations recirculated in the test chamber. Likely, a similar mechanism could affect the current dataset and it will be scrutinized in future campaigns.

Broadband noise is then inspected. Analytical trailing edge noise predictions based on the corrected Schlinker & Amiet's empirical wall pressure model are in fairly good agreement with the PowerFLOW prediction over the whole operational range, with the exception of the hover case, for which the PowerFLOW simulation seems to be slightly over-tripped. Globally, PowerFLOW results are in fair agreement with the measurements over the entire frequency range, although the contamination due to electric motor noise invalidate the current data set in the range 1 to 6 kHz. For the case $J = 0.6$, the measured spectra exhibit a clear hump in the frequency range 4 to 20 kHz, and this is due to the occurrence of a laminar separation bubble. This mechanism is absent in the current tripped/turbulent high-fidelity simulation, as well in the analytical trailing-edge noise formulation.

In order to better illustrate the effect of blade tripping in relation with the occurrence of a laminar bubble at high advance ratio, the noise spectra at microphone #7 for cases $J = 0$ and $J = 0.6$ are compared again in Fig. 22, where the tripped blade measurements are now included. In hover condition, untripped and tripped measurements exhibit a similar high-frequency trend. Conversely, at $J = 0.6$, the high-frequency hump disappears for the tripped case, thus resulting in a difference of more than 10 dB between untripped and tripped blade measurements. The untripped measurements are in very good agreement with the low-fidelity prediction.

Finally, by rearranging the four data sets in a different way in Fig. 23, the spectral trends can be better highlighted and conclusions about the experimental challenges and the capability to predict low-Reynolds number propeller noise using high- and low-fidelity methods can be easily drawn.

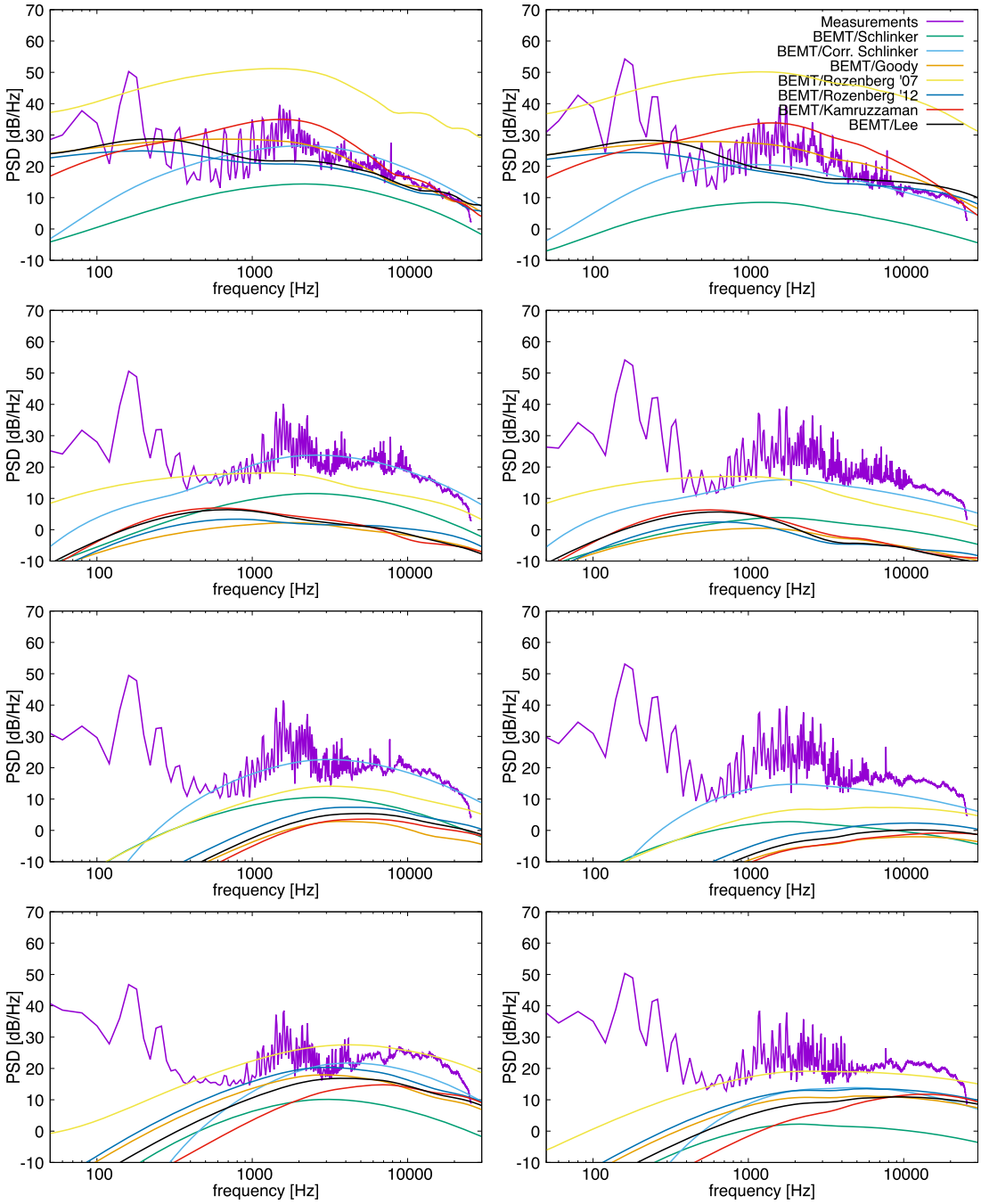

Fig. 13. Noise power spectral density at advance ratios from 0 (top) to 0.6 (bottom) at microphone #1 (left), and #7 (right). Comparison between measurements and semi-analytical broadband results based on different wall pressure models.

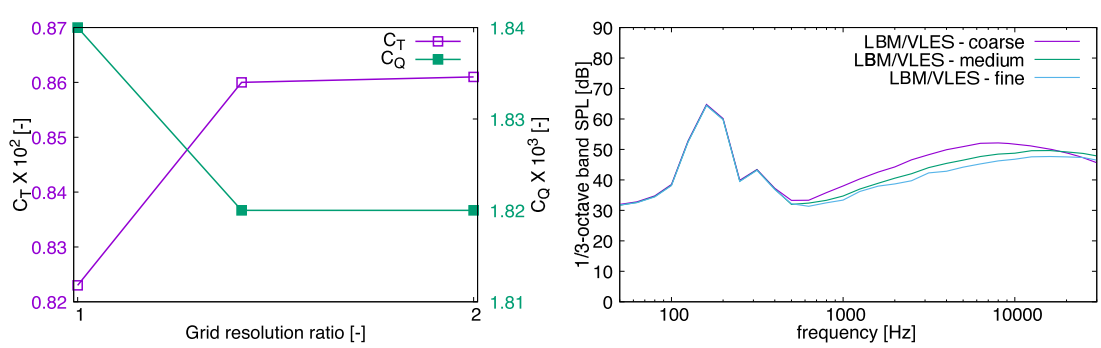

Fig. 14. Effect of mesh resolution on the propeller forces (left) and SPL spectrum at microphone #7 (right) for $J = 0.4$.

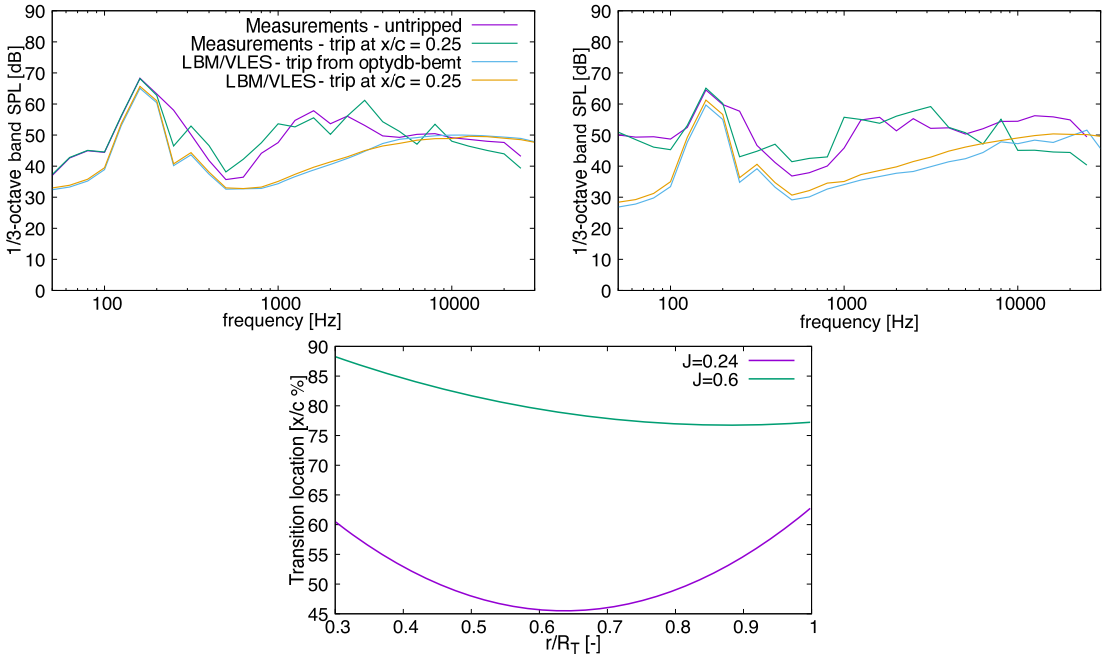

Fig. 15. Effect of trip location on noise spectra at microphone #7; $J = 0.24$ (left), $J = 0.6$ (right) and trip location (bottom).

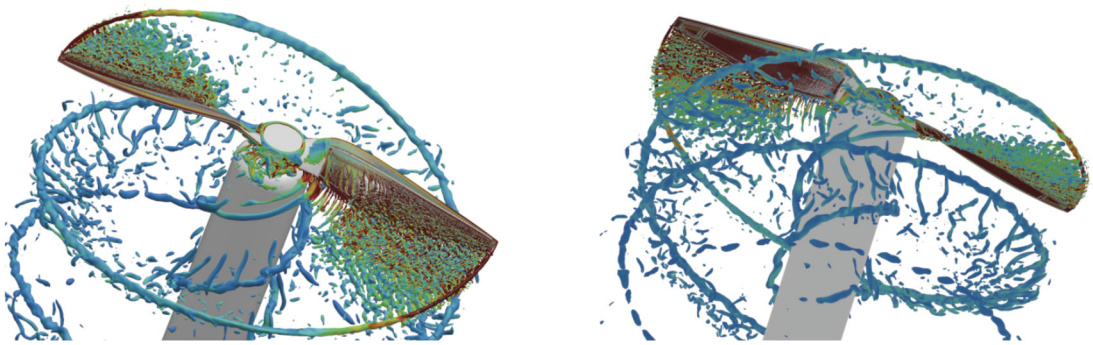

Fig. 16. Iso-surfaces of λ_2 at $J = 0.4$ on the blade suction (left) and pressure side (right).

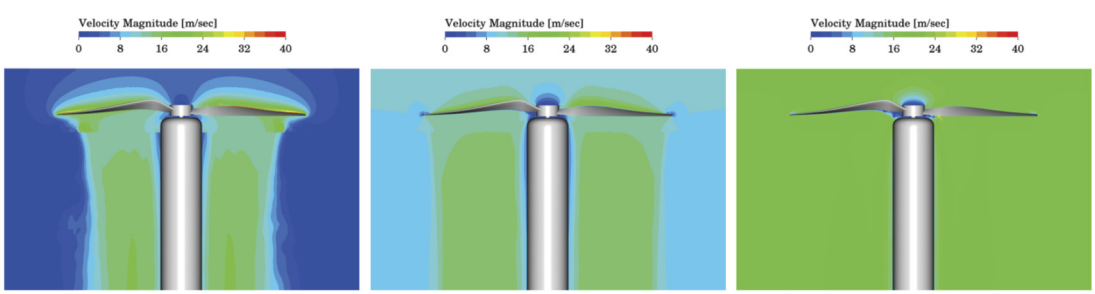

Fig. 17. Time-average velocity magnitude for: $J = 0$ (left), $J = .4$ (middle) and $J = 0.8$ (right).

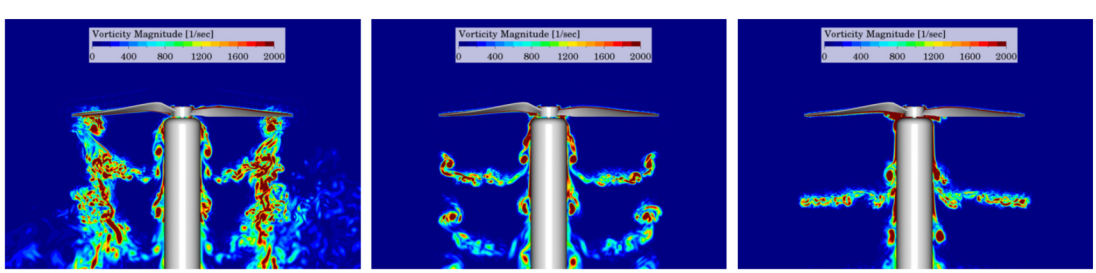

Fig. 18. Instantaneous vorticity magnitude for: $J = 0$ (left), $J = .4$ (middle) and $J = 0.8$ (right).

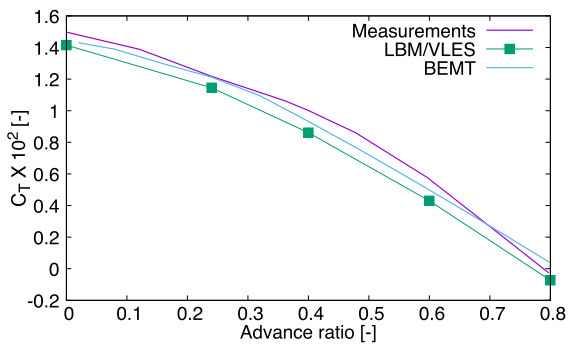

Fig. 19. Thrust coefficient.

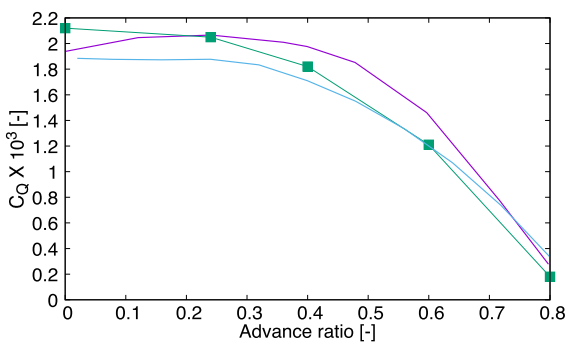

Fig. 20. Torque coefficient.

8. Noise source visualization

As an illustration of some automatic post-processing capabilities of the 3DS eVTOL aeroacoustic workflow, the broadband noise sources are investigated using two complementary approaches. The first one, available in *Opty∂B*-PFNOISESCAN, consists in attributing to every surfel of the blade and at every time step, the noise contribution per unit of surface emitted towards a given microphone. The resulting unsteady surface field is Fourier transformed and then visualized in different integration bands as SPL/m^2. The second approach, based on sequential usage of *Opty∂B*-FWHFREQ and *Opty∂B*-BF, consists in performing a beam-forming analysis for one blade only in the rotating reference system. Noise source maps cumulated over the same frequency ranges for the two analyses are compared, providing some interesting physical insight.

Fig. 24 shows the noise source maps for the blade suction side for three frequency ranges, covering the BPF harmonic count range of 3–10, 10–30 and 30–100. The colour maps range values correspond to the units of dB/m^2 for the time-domain FW-H sources, and to noise power levels referred to the maximum value in a band for the beam-forming maps. These have been computed by using an array of microphones facing the blade suction side, but, due to the intrinsic properties of a wave field, also sources located on the blade pressure side are detected by the source localization algorithm. Indeed, since the microphone used for the FW-H time-domain source projection is located on the pressure side of the propeller (at 5D from the propeller hub and 45° from the propeller plane on the ground side), more consistent beam-forming maps are the ones computed using an array of microphones facing the blade pressure side, which are shown in Fig. 25. A cross checking of the two figures is therefore needed. For the sake of completeness, it should be mentioned that the microphone considered for the FW-H calculation is the first one of the circular array used in Ref. [46], which is at the same directivity angle as the first microphone of the linear array of Fig. 5, but slightly farther from the propeller. Noise levels can be reported to the current array by adding 2 dB.

In the first frequency range, only few sources are detected by the beam-forming on the suction side, whereas the trip self-noise is detected by the beam-forming on the pressure side. This confirms a general observation in airfoil aeroacoustics, according to which the noise radiated towards one side of the airfoil can be more significantly influenced by events happening on the opposite side. It is interesting to observe that one of the two sources detected for the hover case by the suction-side beam-forming array is located in proximity of the leading edge and it should be related to pressure fluctuations induced on the pressure side of the blade by a weak BVI phenomenon occurring in hover conditions, in line with previous observations [1].

In the second frequency range the trailing-edge is more relevant. The suction-side beam-forming maps reveal the dominance of trailing-edge contribution in the form a distributed uncorrelated sources along the edge, with relatively higher noise power levels around a radial station of about 75% for all values of the advance ratio. As already pointed out, the beam-forming array on the pressure side is able to detect the trip self noise.

Finally, in the third frequency range, trailing-edge noise is well evident in the suction-side beam-forming maps, with relatively higher noise power levels around a radial station of about 85% for all values of the advance ratio.

It is worth concluding this section with an observation about one of the intrinsic challenges of aeroacoustics. The surface noise contributions computed using the time-domain FW-H approach represent the effective noise contribution to a given microphone location, with the only caveat of a non-synchronous cumulation due to Doppler effects (the signal reception time is not the same for all surface elements at a given source time due to Doppler effects). However, the SPL contour levels are not able to highlight a specific contribution of the trailing-edge, as beam-forming does. This is because trailing-edge noise is substantially a wave scattering phenomenon and the role of the signal phase in the construction of the radiated field is of fundamental importance. Therefore, sources could be visualized only by looking at the Fourier real/imaginary parts in narrow bands of the same quantity used to compute SPL maps, or through band-pass filtering of the transient field. Conversely, the beam-forming resolves the source interference in a statistical sense, by means of the cross-spectral matrix, and therefore it is able to deliver an equivalent source distribution.

9. Conclusions

A preliminary step towards the definition of a benchmark problem for small UAV propeller aeroacoustics was accomplished through comparisons between measurements and low-/high-fidelity predictions. LBM/VLES simulations were performed by triggering the boundary layer transition on the suction side, without an exact knowledge of the real flow regime in the untripped physical tests. However, the favourable agreements between measured and predicted broadband noise levels supported the presence of a transitional flow regime, at least in the outer part of the blade suction side. This was also confirmed by analytical computations based on a BEMT model which predicted a transition on the suction side, mostly triggered by a laminar separation bubble. The BEMT-predicted transition line on the suction side was located downstream the prescribed quarter-chord location in the LBM/VLES simulations. Additional PowerFLOW simulations with trip following the spanwise transition line predicted by the BEMT revealed that the trip location does not affect the tonal noise content, whereas it affects the high-frequency broadband noise by about 1 dB in hover condition, and up to 10 dB close to zero-thrust conditions, when the transition took place in the last 20%

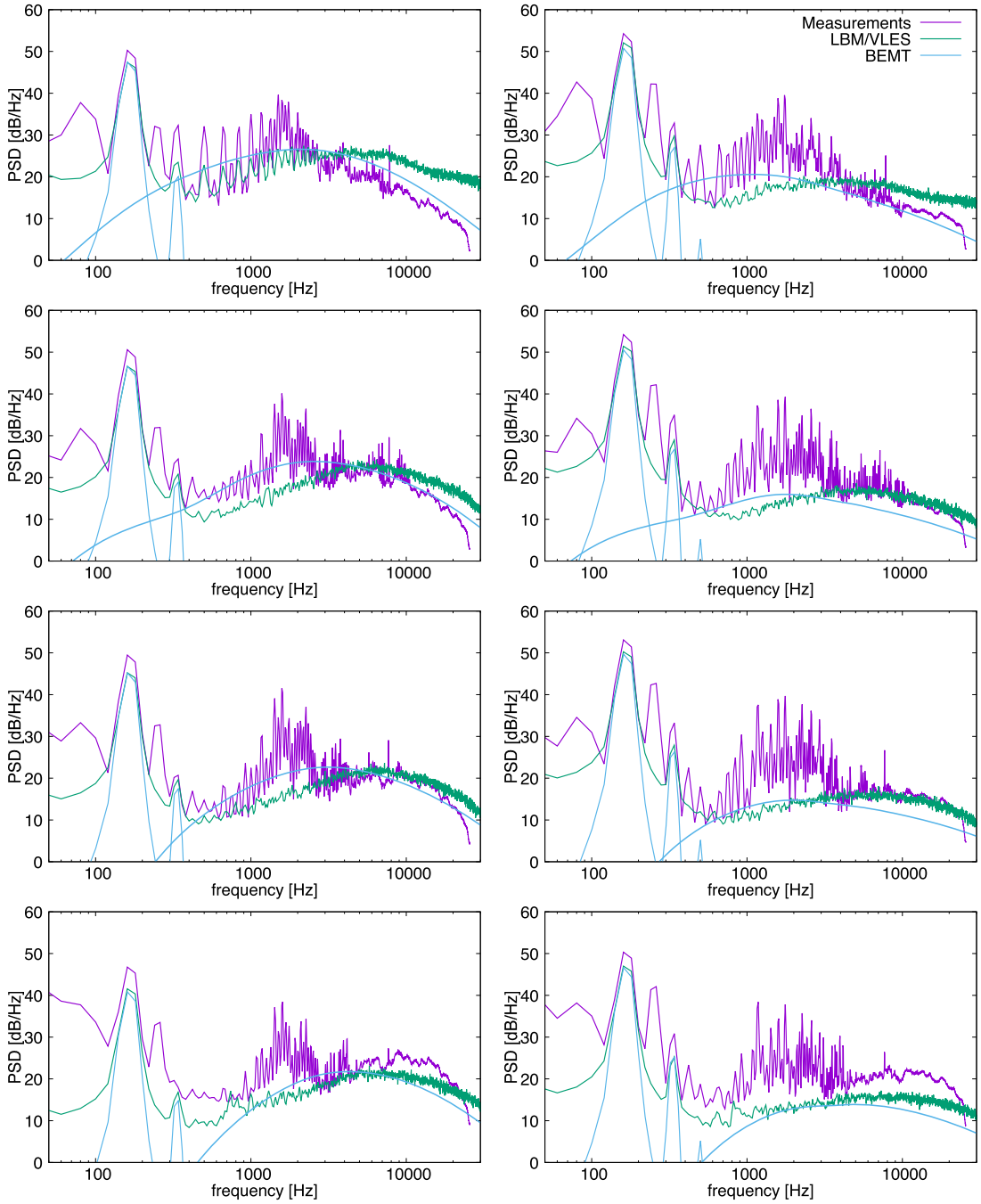

Fig. 21. Noise power spectral density at advance ratios from 0 (top) to 0.6 (bottom) at microphone #1 (left), and #7 (right). Comparison between measurements, BEMT tonal results, semi-analytical broadband results based on corrected Schlinker & Amiet's wall pressure model and PowerFLOW/PowerACOUSTICS results.

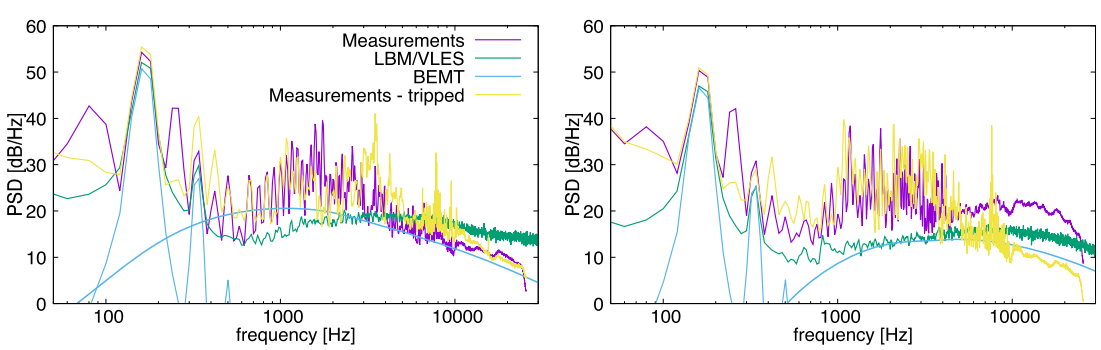

Fig. 22. Noise power spectral density at microphone #7 for two advance ratios: $J = 0$ (left) and $J = 0.6$ (right).

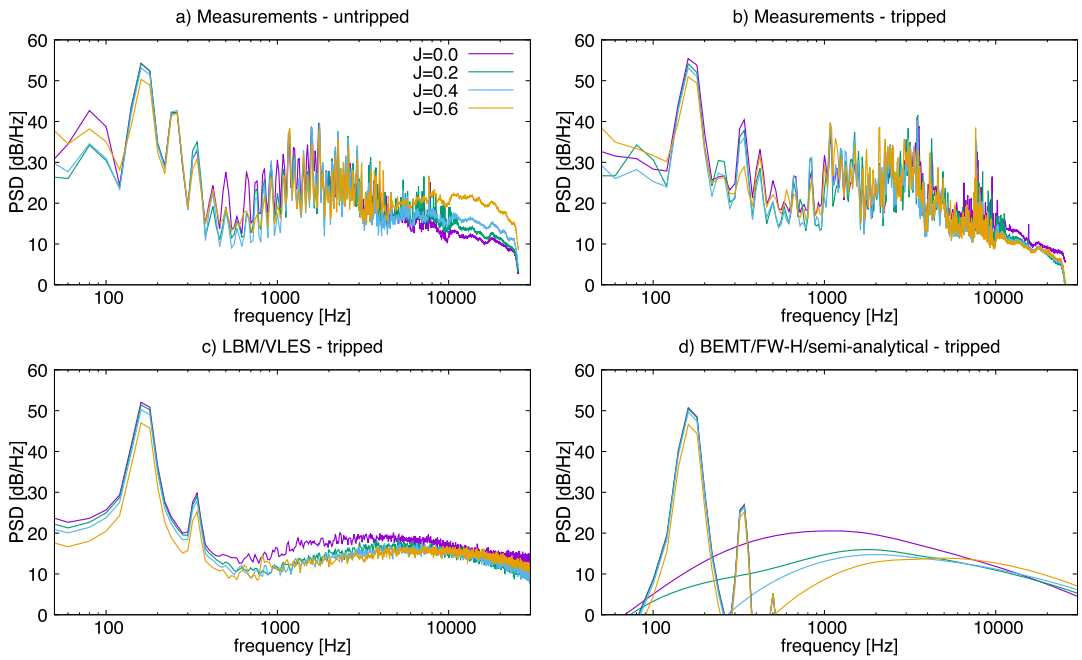

Fig. 23. Noise power spectral density at microphone #7 for all values of the advance ratio.

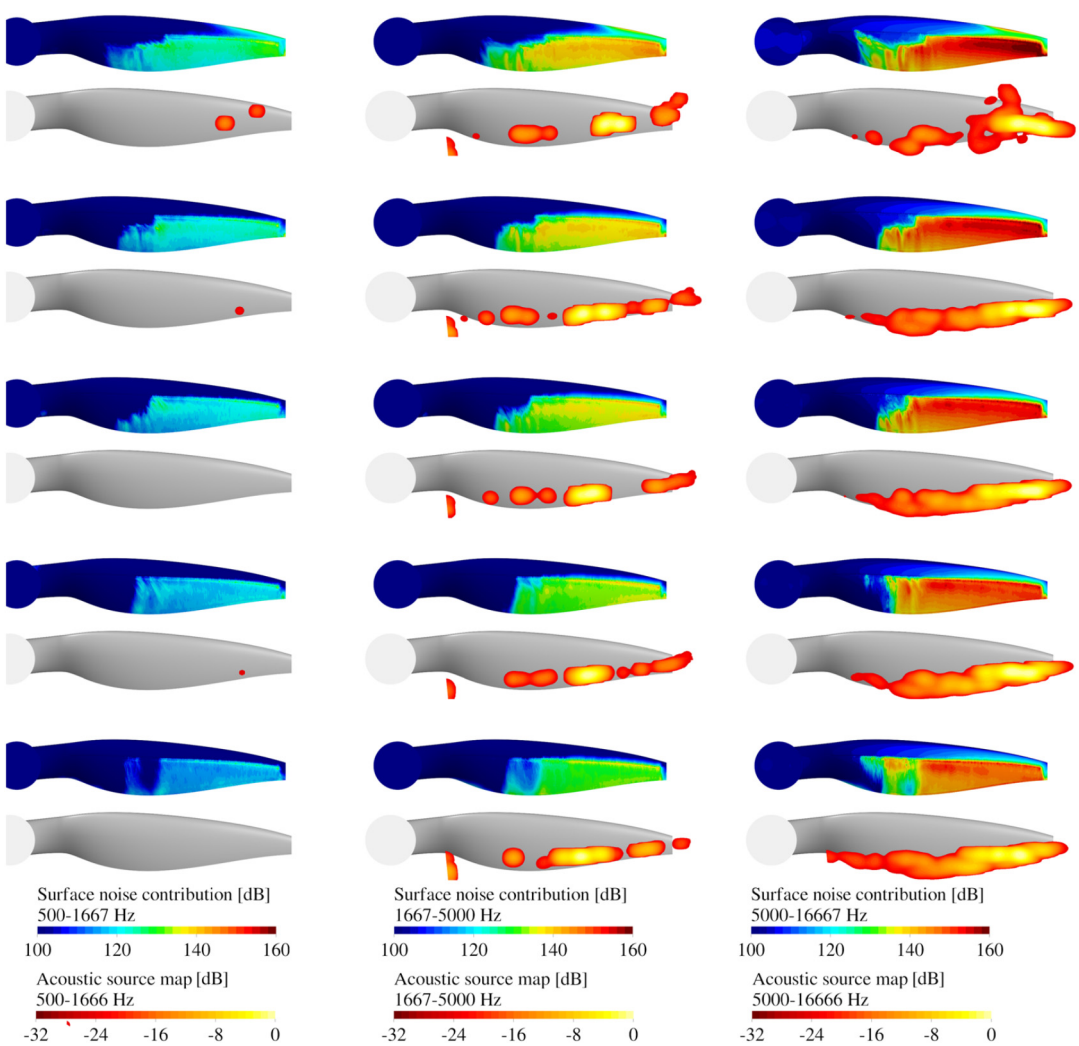

Fig. 24. FW-H integral contribution 45° from the rotor plane and beam-forming noise maps on the blade suction side alternately shown for cases from $J = 0$ (top) to $J = 0.8$ (bottom).

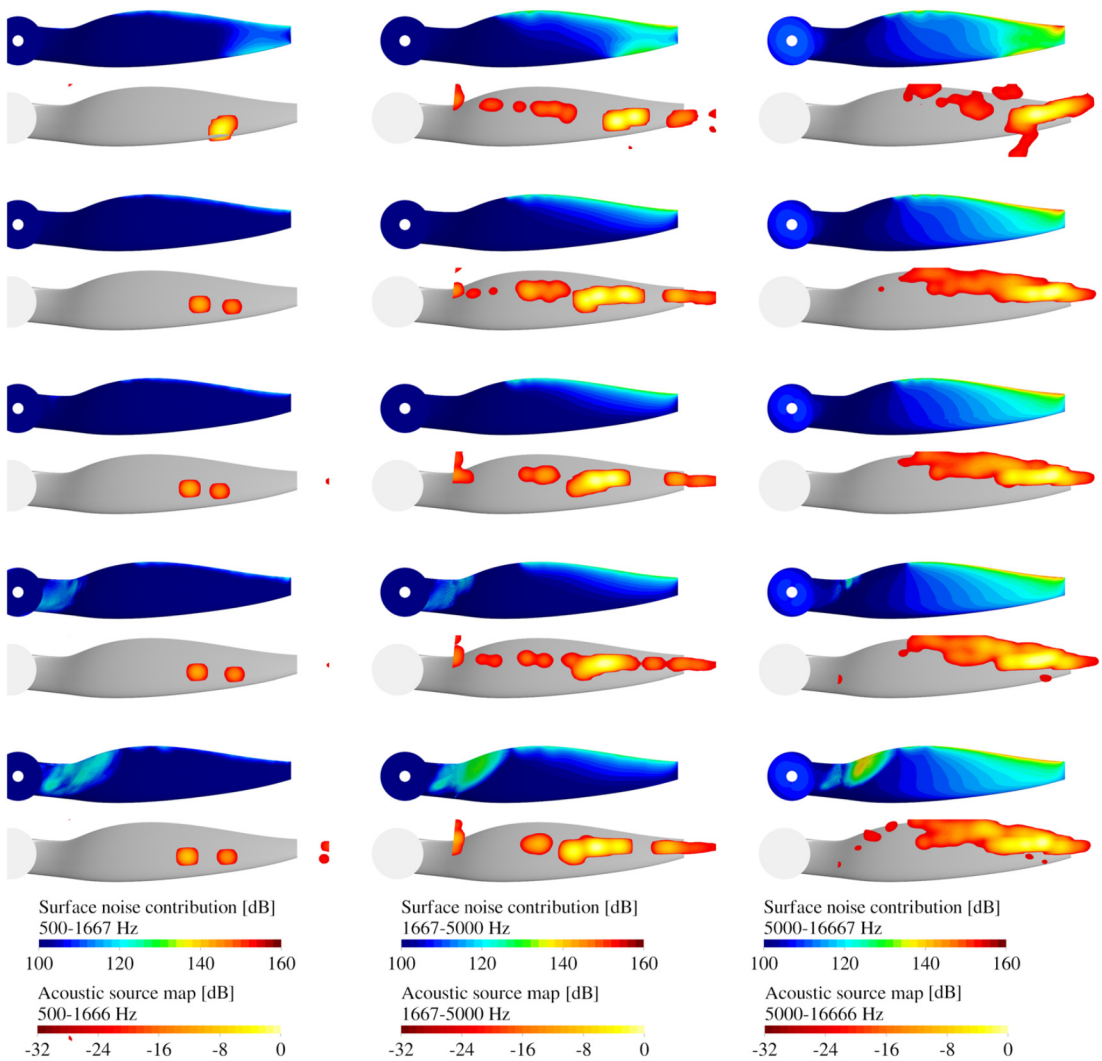

Fig. 25. FW-H integral contribution 45° from the rotor plane and beam-forming noise maps on the blade pressure side alternately shown for cases from $J = 0$ (top) to $J = 0.8$ (bottom).

of the chord along the whole span. The presence of a laminar separation bubble for the higher values of the advanced ratio causing a high-frequency hump in the noise spectrum was confirmed by comparing measurements carried out without and with transition strip on the suction side.

An additional outcome of the present study is the accurate forces and tonal noise prediction carried out using a low-fidelity simulation chain that can be executed in few minutes for many operating conditions. This process coexists with the high-fidelity process and can be reliably used for flight mission and noise assessments. A caveat still exists about the robustness of semi-analytical broadband trailing-edge noise models, due to the sensitivity of the WPS model to the boundary layer properties. The simplest method by Schlinker & Amiet seems to be the most robust one and can be easily tuned to a class of rotor problems.

New experimental campaigns will be conducted in the future with the goal of fixing some of the remaining issues observed during the last campaign, and shed more light on a new research question generated by the present study: the existence of an additional noise generation mechanism due to the presence of a laminar separation bubble and possible tonal noise feedback mechanisms.

Declaration of competing interest

The authors declare that they have no known competing financial interests or personal relationships that could have appeared to influence the work reported in this paper.

References

[1] C. Nardari, D. Casalino, F. Polidoro, V. Coralic, J. Brodie, P.-T. Lew, Numerical and experimental investigation of flow confinement effects on UAV rotor noise, AIAA Paper 2019-2497, 2019.
[2] J.H. Stephenson, D. Weitsman, N.S. Zawodny, Effects of flow recirculation on unmanned aircraft system (UAS) acoustic measurements in closed anechoic chambers, J. Acoust. Soc. Am. 145 (3) (2019) 1153.
[3] R. McKay, M.J. Kingan, Multirotor unmanned aerial system propeller noise caused by unsteady blade motion, AIAA Paper 2019-2499, 2019.
[4] B.S. Henderson, D. Huff, Electric motor noise for small quadcopters, part II: source characteristics and predictions, AIAA Paper 2018-2953, 2018.
[5] D. Casalino, W. van der Velden, G. Romani, Community noise of urban air transportation vehicles, AIAA Paper 2019-1834, 2019.
[6] P. Ventura Diaz, S. Yoon, High-fidelity computational aerodynamics of multi-rotor unmanned aerial vehicles, AIAA Paper 2018-1266, 2018.
[7] P. Batten, U. Goldberg, S. Chakravarthy, Interfacing statistical turbulence closures with large-eddy simulation, AIAA J. 42 (3) (2004) 485–492.
[8] C. Mockett, W. Haase, D. Schwamborn, Go4Hybrid: Grey Area Mitigation for Hybrid RANS-LES Methods, Springer, 2018.
[9] D. Casalino, A. Hazir, A. Mann, Turbofan broadband noise prediction using the lattice Boltzmann method, AIAA J. 56 (2) (2018), https://doi.org/10.2514/1.J055674.

[10] D. Casalino, F. Avallone, I. Gonzalez-Martino, D. Ragni, Aeroacoustic study of a wavy stator leading edge in a realistic fan/OGV stage, J. Sound Vib. 442 (2019) 138–154.
[11] M.L. Shur, P.R. Spalart, M.K. Strelets, A.K. Travin, Synthetic turbulence generators for RANS-LES interfaces in zonal simulations of aerodynamic and aeroacoustic problems, Flow Turbul. Combust. 93 (1) (2014) 63–92.
[12] D. Di Pasquale, A. Rona, S.J. Garrett, A selective review of CFD transition models, AIAA Paper 2019-3812, 2019.
[13] M. Drela, XFOIL: an analysis and design system for low Reynolds number airfoils, in: T.J. Mueller (Ed.), Low Reynolds Number Aerodynamics, in: Lecture Notes in Engineering, vol. 54, Springer, Berlin, Heidelberg, 1989.
[14] O. Gur, A. Rosen, Comparison between blade-element models of propellers, Aeronaut. J. 112 (1138) (2008) 689–704.
[15] D.V. Uhlig, M.S. Selig, Post stall propeller behavior at low Reynolds numbers, AIAA Paper 2008-407, 2008.
[16] M.H. McCrink, J.W. Gregory, Blade element momentum modeling of low-re small UAS electric propulsion systems, AIAA Paper 2015-3296, 2015.
[17] R. Merino-Martinez, A.R. Carpio, L.L. Pereira, S. Herk, F. Avallone, D. Ragni, M. Kotsonis, Aeroacoustic design and characterization of the 3d-printed, open-jet, anechoic wind tunnel of delft university of technology, Appl. Acoust. 170 (2020) 107504.
[18] M. Piellard, B.B. Coutty, V. Le Goff, V. Vidal, F. Perot, Direct aeroacoustics simulation of automotive engine cooling fan system: effect of upstream geometry on broadband noise, AIAA Paper 2014-2455, 2014.
[19] F. Avallone, D. Casalino, D. Ragni, Impingement of a propeller slipstream on a leading edge with a flow-permeable insert: a computational aeroacoustic study, Int. J. Aeroacoust. 17 (2018) 6–8.
[20] I. Gonzalez-Martino, D. Casalino, Fan tonal and broadband noise simulations at transonic operating conditions using lattice-Boltzmann methods, AIAA Paper 2018-3919, 2018.
[21] G. Romani, D. Casalino, Rotorcraft blade-vortex interaction noise prediction using the lattice-Boltzmann method, Aerosp. Sci. Technol. 800 (2019) 147–157.
[22] X. Shan, X.-F. Yuan, H. Chen, Kinetic theory representation of hydrodynamics: a way beyond the Navier-Stokes equation, J. Fluid Mech. 550 (2006) 413–441.
[23] V. Yakhot, S.A. Orszag, Renormalization group analysis of turbulence, I: basic theory, J. Sci. Comput. 1 (1) (1986) 3–51.
[24] M. Pervaiz, C.M. Teixeira, Two equation turbulence modeling with the lattice-Boltzmann method, ASME PVP Am. Soc. Mech. Eng. Press. Vessels Pip. Div. 397 (1999).
[25] H. Chen, S. Orszag, I. Staroselsky, S. Succi, Expanded analogy between Boltzmann kinetic theory of fluid and turbulence, J. Fluid Mech. 519 (2004) 301–314.
[26] F. Farassat, G.P. Succi, The prediction of helicopter discrete frequency noise, Vertica 7 (4) (1983) 309–320.
[27] D. Casalino, An advanced time approach for acoustic analogy predictions, J. Sound Vib. 261 (4) (2003) 583–612.
[28] D.P. Lockard, An efficient, two-dimensional implementation of the Ffowcs Williams and Hawkings equation, J. Sound Vib. 229 (4) (2000) 897–911.
[29] P. Sijtsma, Clean based on spatial source coherence, Int. J. Aeroacoust. 6 (4) (2007) 357–374.
[30] D. Lockard, W. Humphreys, M. Khorrami, E. Fares, D. Casalino, P. Ravetta, Comparison of computational and experimental microphone array results for an 18%-scale aircraft model, Int. J. Aeroacoust. 16 (4–5) (2017) 358–381.
[31] R. van Rooij, W.A. Timmer, Roughness sensitivity considerations for thick rotor blade airfoils, J. Sol. Energy Eng. 125 (4) (2003).
[32] M. Drela, M.B. Giles, Viscous-inviscid analysis of transonic and low Reynolds number airfoils, AIAA J. 25 (10) (1987) 1347–1355.
[33] L.A. Viterna, R.D. Corrigan, Fixed pitch rotor performance of large horizontal axis wind turbines, NASA N83 19233, 1981.
[34] D. Casalino, M. Barbarino, A. Visingardi, Simulation of helicopter community noise in complex urban geometry, AIAA J. 48 (8) (2011) 1614–1624.
[35] M. Roger, S. Moreau, Bach-scattering correction and further extensions of Amiet's trailing edge noise model, part 1: theory, J. Sound Vib. 286 (3) (2005) 477–506.
[36] R.K. Amiet, Frame of reference considerations for the forward flight noise problem, NASA N212775-1, 1974.
[37] R.H. Schlinker, R.K. Amiet, Helicopter trailing edge noise, NASA CR-3470, 1981.
[38] D. Casalino, M. Barbarino, Stochastic method for airfoil self-noise computation in frequency domain, AIAA J. 49 (11) (2011) 2453–2469.
[39] M. Goody, Empirical spectral model of surface pressure fluctuations, AIAA J. 42 (9) (2004) 1788–1794.
[40] Y. Rozenberg, Modélisation analytique du bruit aérodynamique à large bande des machines tournantes: utilisation de calculs moyennés de mécanique des fluides, Ph.D. thesis, Ecole Centrale de Lyon, December 2007.
[41] Y. Rozenberg, G. Robert, S. Moreau, Wall-pressure spectral model including the adverse pressure gradient effects, AIAA J. 50 (10) (2012) 2168–2179.
[42] M. Kamruzzaman, D. Bekiropoulos, T. Lutz, W. Würz, E. Krämer, A semi-empirical surface pressure spectrum model for airfoil trailing- edge noise prediction, Int. J. Aeroacoust. 14 (5–6) (2015) 833–882.
[43] S. Lee, Empirical wall-pressure spectral modeling for zero and adverse pressure gradient flows, AIAA J. 56 (5) (2018) 1818–1829.
[44] Y. Rozenberg, M. Roger, S. Moreau, Rotating blade trailing-edge noise: experimental validation of analytical model, AIAA J. 48 (5) (2010) 951–962.
[45] A. Pagano, M. Barbarino, D. Casalino, L. Federico, Tonal and broadband noise calculations for aeroacoustic optimization of a pusher propeller, J. Aircr. 47 (3) (2010) 835–848.
[46] D. Casalino, E. Grande, G. Romani, D. Ragni, F. Avallone, Towards the definition of a benchmark for low Reynolds number propeller aeroacoustics, in: 18th International Symposium on Transport Phenomena and Dynamics of Rotating Machinery, 2020.
[47] S. Pröbsting, S. Yarusevych, Laminar separation bubble development on an airfoil emitting tonal noise, J. Fluid Mech. 780 (2015) 167–191.
[48] H. Wu, M. Sanjose, S. Moreau, R.D. Sandberg, Direct numerical simulation of the self-noise radiated by the installed controlled-diffusion airfoil at transitional Reynolds number, AIAA Paper 2018-3797, 2018.